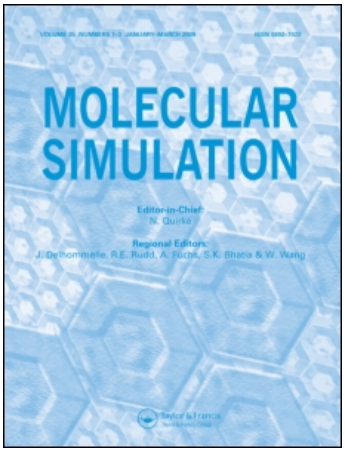

Molecular Simulation

Publication details, including instructions for authors and subscription information:
http://www.informaworld.com/smpp/title~content=t713644482

Thermodynamics of pyrope-majorite, $Mg_3Al_2Si_3O_{12}$-$Mg_4Si_4O_{12}$, solid solution from atomistic model calculations

V. L. Vinograd[a]; B. Winkler[a]; A. Putnis[b]; H. Kroll[b]; V. Milman[c]; J. D. Gale[d]; O. B. Fabrichnaya[e]
[a] Institute of Mineralogy, University of Frankfurt, Frankfurt a.M., Germany [b] Institute of Mineralogy, University of Münster, Münster, Germany [c] Accelrys, Cambridge, UK [d] Nanochemistry Research Institute, Curtin University of Technology, Perth, Australia [e] Max-Planck-Institute for Metal Research, Stuttgart, Germany

To cite this Article Vinograd, V. L. , Winkler, B. , Putnis, A. , Kroll, H. , Milman, V. , Gale, J. D. and Fabrichnaya, O. B.(2006) 'Thermodynamics of pyrope-majorite, $Mg_3Al_2Si_3O_{12}$-$Mg_4Si_4O_{12}$, solid solution from atomistic model calculations', Molecular Simulation, 32: 2, 85 — 99
To link to this Article: DOI: 10.1080/08927020500501599
URL: http://dx.doi.org/10.1080/08927020500501599

Molecular Simulation, Vol. 32, No. 2, 15 February 2006, 85–99

Thermodynamics of pyrope–majorite, $Mg_3Al_2Si_3O_{12}$–$Mg_4Si_4O_{12}$, solid solution from atomistic model calculations

V. L. VINOGRAD†*, B. WINKLER†, A. PUTNIS‡, H. KROLL‡, V. MILMAN¶, J. D. GALE§ and O. B. FABRICHNAYA‖

†Institute of Mineralogy, University of Frankfurt, Senckenberanlage 30, 60054 Frankfurt a.M., Germany
‡Institute of Mineralogy, University of Münster, Corrensstrasse 24, 48149 Münster, Germany
¶Accelrys, 334 Cambridge Science Park, Cambridge CB4 0WN, UK
§Nanochemistry Research Institute, Curtin University of Technology, PO Box U1987, Perth WA 6845, Australia
‖Max-Planck-Institute for Metal Research, Heisenbergstr. 3, 70569 Stuttgart, Germany

(Received October 2005; in final form December 2005)

Static lattice energy calculations, based on empirical pair potentials have been performed for a large set of different structures with compositions between pyrope and majorite, and with different states of order of octahedral cations. The energies have been cluster expanded using pair and quaternary terms. The derived ordering constants have been used to constrain Monte–Carlo simulations of temperature-dependent properties in the ranges of 1073–3673 K and 0–20 GPa. The free energies of mixing have been calculated using the method of thermodynamic integration. At zero pressure the cubic/tetragonal transition is predicted for pure majorite at 3300 K. The transition temperature decreases with the increase of the pyrope mole fraction. A miscibility gap associated with the transition starts to develop at about 2000 K and $x_{maj} = 0.8$, and widens with the decrease in temperature and the increase in pressure. Activity–composition relations in the range of 0–20 GPa and 1073–2673 K are described with the help of a high-order Redlich–Kister polynomial.

Keywords: Pyrope–majorite s.s.; Monte–Carlo simulations; Cubic/tetragonal transition; Activity–composition relations

1. Introduction

Recent progress in the understanding of the chemical composition and thermo-physical properties of the Earth's mantle has been achieved by comparing geophysical data on seismic velocities with the corresponding properties of theoretically calculated equilibrium mineral assemblages subjected to high pressures and temperatures [1]. Pyrope- and majorite-rich garnet is thought to be an important phase of variable composition in the transition zone of the Earth's mantle (410–650 km). Theoretical calculations show [2,3] that the mole fraction of majorite, $Mg_4Si_4O_{12}$, component in the aluminosilicate garnet increases gradually with depth. This corresponds to an increase of the site fractions of Mg and Si in the octahedral position of the garnet structure, which occurs via the coupled substitution $2Al^{3+} = Mg^{2+} + Si^{4+}$. Any realistic model of mineral transformations in the transition zone requires knowledge of the thermodynamic activities of pyrope and majorite in the garnet solid solution. This study is concerned with atomistic modelling of thermodynamic mixing effects associated with this substitution.

Due to practical challenges, few experimental data is available to constrain the thermodynamics of mixing in the pyrope–majorite binary system. Akaogi *et al.* [4] have determined heats of dissolution in molten $2PbO{*}B_2O_3$ of several cubic garnets with compositions in the range of $0 < x_{maj} < 0.58$. They have observed an approximately linear variation of the heat of dissolution in this compositional range. The dissolution enthalpy of the majorite end-member with the tetragonal structure has been measured by Yusa *et al.* [5]. Using a linear extrapolation of the data of Akaogi *et al.* [4], Yusa *et al.* [5] have estimated the enthalpy of the cubic/tetragonal transition in majorite to be 20.4 ± 5.0 kJ/mol per 12 oxygen atoms. The combination of the data of Akaogi *et al.* [4] and Yusa *et al.* [5] suggests a positive enthalpy of mixing at intermediate compositions with a value of about 12 ± 3.0 kJ/mol at $x_{maj} = 0.6$. Phase equilibrium studies cannot be used to tightly constrain mixing properties due to large uncertainties in the pressure calibration and in the equilibrium composition of the garnet phase. The reported maximal solubility of majorite in garnet in an assemblage with wadsleyite and stishovite varies between different

*Corresponding author. Tel.: +49-69-798-22764. E-mail: v.vinograd@kristall.uni-frankfurt.de

Molecular Simulation
ISSN 0892-7022 print/ISSN 1029-0435 online © 2006 Taylor & Francis
http://www.tandf.co.uk/journals
DOI: 10.1080/08927020500501599

studies by up to 20 mole%. [6,7]. However, the lack of thermodynamic data is partially compensated by an abundance of structural information. It is known that pure majorite at low temperatures crystallizes in the tetragonal space group $I4_1/a$ [8]. Pyrope-rich compositions have a cubic structure with space group $Ia\bar{3}d$. The cubic/tetragonal transition is caused by long-range ordering of Mg and Si in the octahedral site. Majorite samples synthesized at 1800°C, 17 GPa [9] and at 2000°C, 17.7 GPa [10] show nearly complete Mg/Si order. Heinemann *et al.* [11] have located the cubic/tetragonal transition at $x_{maj} = 0.8$ in samples synthesized at 2000°C and 19 GPa. However, Heinemann *et al.* [11] and Hatch and Ghose [12] noted that the true temperature of the order/disorder transition cannot be judged based on the synthesis temperatures. The tetragonal majorites are twinned, thereby suggesting that they have a higher symmetry precursor. Heinemann *et al.* [11] and Hatch and Ghose [12] argued, therefore, that the cubic/tetragonal transition occurs during the quench and thus the transition boundary lies somewhere below 1800°C. This assumption has been questioned by Wang *et al.* [13], who have observed tweed microstructure in majorite-rich samples synthesized at 2300°C, just below the melting temperature, which is about 2600°C for pure majorite [14]. Wang *et al.* [13] concluded that the transition occurs at about 2300°C. The location of the transition boundary is a matter of an ongoing debate [15], which has important implications for models of the rheological properties of the transition zone. If the stability field of tetragonal majorite-rich garnets is intersected by the mantle geotherm, it is most likely that the elastic properties of majorite are altered due to the presence of mobile domain walls. For example, a drastic change in the viscoelasticity due to the cubic/tetragonal transition has recently been observed experimentally in $Ca_{1-x}Sr_xTiO_3$ perovskite [16]. Heinemann *et al.* [11] have noted that the increase of the pyrope mole fraction should enhance disorder on octahedral sites and move the transition to even lower temperatures, thus decreasing the likelihood for an intersection of the $I4_1/a$ stability field by the geotherm. In this sense, the pyrope–majorite system behaves then analogously to the plagioclase solid solution where an increase in the albite mole fraction leads to a rapid decrease of the $C\bar{1}/I\bar{1}$ transition temperature [17]. Referring to the same analogy, one can expect that the mixing enthalpy has a kink at the transition line and that a miscibility gap, associated with the boundary, develops at some low temperature. Such a gap should be reflected in the thermodynamic activities of pyrope and majorite. The commonly used "two sublattice" model [4,5,14] ignores this complication. In this model, the configurational entropy related to the octahedral atoms is assumed to be ideal for the Mg-rich and Si-rich sublattices, i.e. Al is allowed to mix randomly either with Mg in the Mg-rich sublattice or with Si in the Si-rich sublattice. Being consistent with the complete long-range order (LRO) in pure majorite, the "two sublattice" model offers a reasonable approximation for the configurational entropy of well ordered tetragonal samples. However, the application of this model to pyrope-rich cubic garnets cannot be easily justified: In the cubic phase Mg, Si and Al should be allowed to mix within the same sublattice. Since the composition of the majoritic garnet widely varies in different Mg–Al–Si–O mineral assemblages [3,4], it is desirable to develop a model which is applicable to the whole compositional range and to both cubic and tetragonal garnets. Based on empirical static lattice energy and quantum mechanical total energy calculations, as well as Monte–Carlo modelling, this study aims to constrain the cubic/tetragonal transition and mixing properties along the pyrope–majorite binary in the pressure and temperature range relevant for the transition zone.

2. Simulation methodology

The methodology we adopt in this study has been established in a series of recent simulation studies [18–24]. It consists of the following steps:

- Development and testing of a set of empirical interatomic potentials.
- Static lattice energy calculations (SLEC) on a set of structures with randomly varied cation configurations.
- Finding a simple equation that describes the energies of the simulated structures. This procedure is known as the "cluster expansion".
- Using the cluster expansion model to obtain temperature-dependent properties by Monte–Carlo simulation.
- Calculation of the free energies of mixing and ordering by thermodynamic integration of the Monte–Carlo results.
- Refitting the free energies to simple polynomial equations useful for phase equilibrium calculations.

2.1 The empirical potentials

A set of empirical interatomic potentials has been developed in this study using the relax-fitting procedure [25] as implemented in the GULP program [26]. The set involves two-parameter Metal–Oxygen (M–O) Buckingham potentials, three-body O–M–O angle-bending terms and the shell model for the oxygen polarisability [27–29]. Following Vinograd *et al.* [30], we have multiplied formal cation and anion charges by the common factor 0.85, so that the charges of Mg, Al, Si and O have been reduced to the values of 1.7, 2.55, 3.4 and − 1.7, respectively. Such a reduction leads to a much better transferability of the potentials within mono- and complex oxides. The possible reason for this improvement is that in dense structures the formal charges on cations cause too strong a cation–cation repulsion. Vinograd *et al.* [30] noted that the cation–cation distances tend to be too long in the formal-charge models. The reduction of the charges by a small common factor removes this problem, but conveniently preserves the charge balance.

Table 1. The empirical interatomic potentials used in the present study. The notation [4] and [6] refers to the coordination number of the associated species.

Interaction	*A* *(eV)*	*ρ* *(Å)*	*C* *(eV* Å^6)*
Buckingham			
Al(core)–O(shell)	1262.2081	0.286370	0.0
Mg(core)–O(shell)	1432.8544	0.277265	0.0
Si(core)–O(shell)	1073.4668	0.298398	0.0
O(shell)–O(shell)	598.8996	0.314947	26.89746
Spring			
	K (eV* Å^{-2})		
O(core)–O(shell)	56.5598		
Three-body			
	k_θ (eV*rad^{-2})	θ (degree)	
O(shell)–Si[4]– O(shell)	0.77664	109.47	
O(shell)–Si[6]– O(shell)	2.2955	90.0	
O(shell)–Al[4]– O(shell)	1.2883	109.47	
O(shell)–Al[6]– O(shell)	1.8807	90.0	

Note: The charges on the oxygen core and shell are 0.746527 and −2.446527, respectively. Cutoff distance for the Buckingham potentials is 12 Å.

The Buckingham Si(core)–O(shell) and O(core) – O(shell) potentials have been fitted to structural and elastic constants of stishovite, coesite and α-quartz. The Al–O potential has been fitted to the data on corundum and the three Al_2SiO_5 polymorphs. The Mg–O potential has been fitted to the data on periclase, spinel ($MgAl_2O_4$), forsterite, wadsleyite, ringwoodite, ilmenite, perovskite, pyrope and cordierite. The three-body terms have then been refitted to relevant subsets of the above-mentioned minerals. The elastic constants have been adopted from the compilation of Bass [31]. The structural constants have been taken from the online American Mineralogist Crystal Structures Database [32]. The potential set is reproduced in table 1. Table 2 compares the predicted and observed structural and elastic parameters of majorite. The data for majorite have not been included in the fit, and therefore can be used as a test of the transferability and accuracy of the potentials.

2.2 Quantum mechanical calculations as a test for the accuracy of the potentials

While calculations based on empirical potentials are computationally very efficient, the predictive power of this approach requires an independent test. Here, we compare selected SLEC results with parameter-free quantum mechanical calculations. For crystals, most quantum mechanical calculations are currently based on the density functional theory (DFT) [35–39]. While DFT itself is exact [35], practical calculations require an approximation for the treatment of the exchange and correlation energies. Here, we use the generalized gradient approximation (GGA), in the form suggested by Perdew *et al.* [40]. Results based on GGA calculations are generally in better agreement with experiment than those obtained with the local density approximation, LDA [41–43]. The study of structures with large unit cells requires a computationally efficient approach. Here, we use the computational scheme in which the charge density and electronic wave functions are expanded in a basis set of plane waves. To avoid explicit description of tightly bound core electrons, the approach employs "ultrasoft" pseudopotentials [44,45] which mimic the screening of the Coulomb potential of the nucleus by the core electrons.

Both the academic and commercial versions of CASTEP were used in the present study for the DFT–GGA calculations. The cut-off energy for the plane wave expansion was 380 eV. Calculations were performed for ordered tetragonal $I4_1/a$ majorite, using the primitive cell and a k-point sampling of $4 \times 4 \times 4$. In all calculations, all symmetry independent structural parameters were varied simultaneously in the search for the ground state geometry. The parameters of the "relaxed" (optimized) structure are given in table 2 and figure 1 where they are compared to experimental values and to the results of the calculations based on empirical potentials. We also computed the ground state structures of cubic, $P4_1$ 32 majorite, $Ia\bar{3}d$ pyrope and the intermediate, Maj50, structure with $Ia\bar{3}$ symmetry in order to compare the differences of their total energies to those of the static lattice empirical–potential based calculations. Table 3 shows the differences in the lattice energy between the configurations of the same composition. The difference in energies of the cubic $P4_1$ 32 and tetragonal $I4_1/a$ majorites constitutes 0.105 eV (10.2 kJ/mol) and 0.156 eV (15.0 kJ/mol) for the SLEC and *ab initio* calculations, respectively. The energy of the intermediate structure $Ia\bar{3}$ is larger than the energy of the equal mixture of pyrope and tetragonal, $I4_1/a$, majorites by 4.9 kJ/mol (SLEC) and by 7.2 kJ/mol (DFT GGA). These results show that the *ab initio* and SLEC results are consistent with each other, but also point to the limitations of these methods. The differences in the results could be due to limited transferability of the empirical potentials and due to the "underbonding" usually observed in DFT GGA calculations. DFT GGA calculations slightly overestimate lattice parameters, which is also seen in the present results for $I4_1/a$ majorite ($a = 11.67$ Å, $c = 11.56$ Å). Figure 1 shows that the distances of short Si–O and Mg–O bonds, predicted *ab initio*, are in a very good agreement with the experiment, while the length of Mg–O bonds with distances larger that 2.3 Å is exaggerated. In view of these limitations, the 30% difference between the SLEC and DFT GGA could be considered reasonable. The atomic coordinates and bond distances calculated with the SLEC agree well with the data of Angel *et al.* [9]. However, the *a*/*c* ratios calculated with the SLEC and DFT GGA disagree with the very small ratio reported by Angel *et al.* [9]. On the contrary, our results compare well with the ratios reported by Kato and Kumazawa [8], Heinemann *et al.* [11] and McCommon and Ross [46]. In summary, we conclude that the new potentials predict reasonable structural parameters and reasonable energy differences between the structures selected for the *ab initio* test. These potentials will be used below to predict the energies of a larger set of structures different in the composition and the state of order.

Table 2. Structural data and elastic stiffness coefficients for majorite as calculated with the SLEC and DFT GGA in comparison with available experimental data.

Cell parameters		*XRD*	*SLEC*	*DFT–GGA*
a (Å)		11.501[a]; 11.481[b]; 11.519[c]	11.494	11.670
c (Å)		11.48[a]; 11.406[b]; 11.420[c]	11.392	11.561
a/*c*		1.0018	1.0089	1.0094
Volume (Å^3)		1518.494 [a]	1505.040	1574.474
Atomic coordinates				
		XRD[a]	SLEC (Core)	DFT–GGA
Mg1 16f	*x*	0.1253	0.1256	0.1287
	y	0.0112	0.0120	0.0135
	z	0.2587	0.2623	0.2665
Mg2 8e	*x*	0.0000	0.0000	0.0000
	y	0.2500	0.2500	0.2500
	z	0.6258	0.6227	0.6235
Mg3 8c	*x*	0.0000	0.0000	0.0000
	y	0.0000	0.0000	0.0000
	z	0.5000	0.5000	0.5000
Si1 4a	*x*	0.0000	0.0000	0.0000
	y	0.2500	0.2500	0.2500
	z	0.3750	0.3750	0.3750
Si2 4b	*x*	0.0000	0.0000	0.0000
	y	0.2500	0.2500	0.2500
	z	0.8750	0.8750	0.8750
Si3 16f	*x*	0.1249	0.1261	0.1254
	y	0.0065	0.0116	0.0116
	z	0.7544	0.7560	0.7568
Si4 8d	*x*	0.0000	0.0000	0.0000
	y	0.0000	0.0000	0.0000
	z	0.0000	0.0000	0.0000
O1 16f	*x*	0.0282	0.0257	0.0268
	y	0.0550	0.0603	0.0588
	z	0.6633	0.6685	0.6691
O2 16f	*x*	0.0380	0.0429	0.0447
	y	0.9529	0.9540	0.9565
	z	0.8562	0.8610	0.8611
O3 16f	*x*	0.2195	0.2248	0.2234
	y	0.1023	0.1079	0.1069
	z	0.8021	0.8070	0.8053
O4 16f	*x*	0.2150	0.2145	0.2117
	y	0.9106	0.9161	0.9165
	z	0.7000	0.7013	0.7028
O5 16f	*x*	0.9412	0.9353	0.9372
	y	0.1617	0.1629	0.1638
	z	0.4680	0.4690	0.4678
O6 16f	*x*	0.8960	0.8980	0.8977
	y	0.2080	0.2102	0.2153
	z	0.7851	0.7821	0.7833
Elastic constants				
	Observed (GPa)	SLEC (GPa)		
C_{11}	286.4[d]	295.10		
C_{44}	85.0[d]	85.23		
C_{66}	93.2[d]	93.66		
C_{12}	83.0[d]	112.7		
C_{16}	1.4[d]	14.72		
Bulk modulus	159.8[d]; 166.0[e]	170.14		

[a]Angel *et al.* [9]; [b]Kato and Kumazawa [8]; [c]Heinemann *et al.* [11]; [d]Pacalo and Weidner [33]; [e]Sinogeikin and Bass [34].

2.3 Supercell calculations

The SLEC calculations have been performed in the athermal limit with GULP in a 2 × 2 × 2 supercell (128 octahedral sites) on set of specially constructed structures (configurations) with different compositions and ordering states. In the first set of calculations, the pressure was fixed at 0 GPa. We have started with the ordered octahedral arrangement of Mg and Si consistent with the $I4_1/a$ structure determined by Angel *et al.* [9] and calculated its relaxed energy. The relaxed coordinates have been used as starting values for a new structure in which one randomly chosen pair of Mg and Si was swapped. The swapping has been repeated 60 times. During this exercise, the static energy increased sharply during the initial steps. Then the rate of increase slowed down indicating the approach to

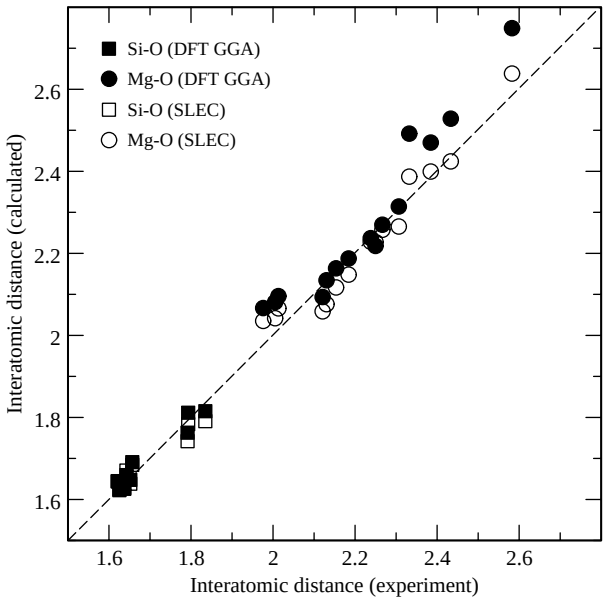

Figure 1. A plot of the predicted interatomic distances against the experimental data of Angel *et al.* [9].

a set of random distributions. The 60 generated structures with variable degrees of disorder have been added to the data base. The same procedure has been repeated for structures with the compositions $x_{\mathrm{maj}} = 0.75$, 0.50 and 0.25, respectively, which have been prepared from $I4_1/a$ majorite by replacing appropriate numbers of Mg and Si with Al atoms. The whole set of configurations was used again in a further set of force field calculations at 20 GPa.

2.4 Cluster expansion

The aim of the cluster expansion is to find a simple equation, which fits the energies (or enthalpies in the case of a nonzero pressure) of all simulated configurations and, hopefully, predicts the energy of any other possible configuration. One popular form for such an expansion is known as the *J*s formalism [19,47],

$$E_i \approx \frac{1}{2}\sum_n z^{(n)} P_{\mathrm{AB}^{(n)}} J_n + E_0 \qquad (1)$$

where $z^{(n)}$, $P_{\mathrm{AB}^{(n)}}$, J_n are the coordination numbers, frequencies of AB-type pairs and ordering constants for pairs of the order *n*. J_n corresponds to the energy (or enthalpy) of the exchange reaction

$$\mathrm{AA} + \mathrm{BB} = 2\mathrm{AB} \qquad (2)$$

Table 3. The comparison between empirically and *ab initio* calculated differences in the lattice energies of selected configurations.

Energy difference	*Empirical potentials*	*Ab initio*
D − (A + B)/2	0.0508	0.0744
C–B	0.1054	0.1556

Notations: A—pyrope, $Ia\bar{3}d$; B—majorite, $I4_1/a$; C—Majorite, $P4_132$; D—Majorite50, $Ia\bar{3}$. Values are in eV per octahedral atom.

between atoms A ∈ {Al, Mg, Si} and B ∈ {Al, Mg, Si} located at the *n*-th distance. When this equation is applied to the excess energies, E_0 is either assumed to be equal to zero [23] or fitted together with the *J*s [24]. In order to determine the set of the *J*s for each of the 240 structures prepared in the way described above we have calculated the frequencies of occurrence of pairs of dissimilar atoms at 8 distances, as specified in table 4. Since there are 3 types of dissimilar pairs, Mg–Si, Mg–Al, and Al–Mg, each configuration *i* is characterized by 24 frequencies, P_n (the factor $1/2z^{(n)}$ is included in the frequency value), and by a value of the relaxed excess energy E_i, where the excess value is defined relative to the weighted sum of the relaxed energies of pyrope and $I4_1/a$ majorite. The whole set of configurations has been thus characterized by the 240 × 24 frequency matrix **P** and with the 240-element vector **E**. With each dissimilar pair we associate a constant J_n. The vector **J** is traditionally found by solving the matrix equation $\mathbf{J} = \mathbf{P}^{-1}\mathbf{E}$ using a least squares method. We adopt here a slightly different technique. Vinograd *et al.* [24] in the study of pyrope–grossular system have observed that when the fit is applied separately to configurations of the same composition, the E_0 value varies with the composition non-linearly. It was shown that this variation can be well approximated with a Margules two-parameter equation

$$E_0 = x_1 x_2 (x_1 A_{12} + x_2 A_{21}) \qquad (3)$$

where x_i are the mole fractions of the end-members. Physically, E_0 describes the energy, which is required to prepare a virtual crystal from the two end-members. In the virtual crystal the exchangeable atoms, Mg, Al, and Si are "homogenized" forming a virtual atom with the average size and charge. The state of the virtual crystal is the reference state of the *J*s expansion. The *J*s describe the energetic advantage of separating pairs of virtual atoms into the pairs of dissimilar atoms and thus include bond relaxation effects and the Coulomb interaction. In the case of the pyrope–majorite solid solution the mixing of the cations occurs not only in the solution, but also at the end-member (majorite) composition. Therefore, E_0 does not vanish at $x_2 = 1$, but includes the energy of homogenization of Mg^{2+} and Si^{4+}. To take into account the non-zero value of E_0 for majorite, we modify equation (3) as follows

$$E_0 = y_1 y_2 (y_1 A_{12} + y_2 A_{21}) \qquad (4)$$

where $y_2 = x_2/2 = X_{\mathrm{maj}}/2$ and $y_1 = 1 - y_2$. Since E_0 is a configuration-independent term, its value must not be mapped onto the *J*s expansion. Therefore, the **J** vector is found from $\mathbf{J} = \mathbf{P}^{-1}\mathbf{E}'$, where the vector $\mathbf{E}'$ is obtained from the vector **E** by subtracting the value of E_0 from each element. Within this procedure we calculate the vector E'', which represents the approximation to E' predicted with the *J*s expansion. Finally, we search for the values of A_{12} and A_{21}, which result in the best fit. The set of the J_n and A_{ij} parameters is then used to calculate energies of configurations within a Monte–Carlo algorithm. However,

Table 4. The final parameters of the fitted cluster expansion.

	0 GPa			*20 GPa*		
Distance (Å)	*Mg–Al*	*Al–Si*	*Mg–Si*	*Mg–Al*	*Al–Si*	*Mg–Si*
Pairwise energies						
4.9511	−13.849	−12.332	−32.350	−21.125	−21.611	−54.338
5.7178	−17.769	−16.637	−46.718	−20.852	−18.233	−51.553
8.0883	−9.239	−8.113	−16.804	−11.700	−9.697	−24.627
9.4852	−6.203	−4.772	−8.486	−7.239	−4.259	−13.335
9.9072	−4.526	−3.923	−5.208	−7.152	−3.093	−8.592
11.4400	−2.321	−3.344	−5.148	−5.540	−6.009	−7.435
12.4676	−2.948	−0.165	0.664	−7.252	−3.375	−1.886
12.7916	−2.093	−1.855	−1.742	−4.913	−1.385	−2.286
The elastic term						
Parameter	0 GPa	20 GPa				
A_{12}	610.85	906.51				
A_{21}	640.00	899.48				
Quaternary energies						
Cluster type	0 GPa	20 GPa				
MgMgMgSi	−3.8054	−4.0740				
MgSiMgSi	−12.7228	−14.4620				
MgSiSiSi	−3.3496	−4.3289				
AlAlAlSi	2.7180	1.0271				
AlAlSiSi	5.0292	3.2307				
AlSiAlSi	−2.0462	−3.1154				
AlSiSiSi	1.6866	2.3576				
AlAlAlMg	−0.8564	−0.0710				
AlAlMgMg	0.0363	2.2000				
AlMgAlMg	−6.4528	−6.8823				
AlMgMgMg	−1.7643	−2.1405				
MgAlSiSi	2.1632	1.0320				
MgSiAlSi	−7.2655	−4.7004				
AlSiMgMg	−0.4698	0.0186				
AlMgSiMg	−5.8033	−7.8190				
MgSiAlAl	0.0	0.0				
MgAlSiAl	0.0	0.0				
MgMgSiSi	0.0	0.0				
MgMgMgMg	0.0	0.0				
SiSiSiSi	0.0	0.0				
AlAlAlAl	0.0	0.0				

Note: the values are in kJ per mole of octahedral cations, or per 1.5 moles of $Si^{[4]}$ atoms.

experience shows that the *J*s calculated in the described way often predict wrong ground states. In order to avoid this problem we have designed a feedback algorithm (figure 2) in which the *J*s self-educate to predict the correct ground state. The algorithm involves a Monte–Carlo annealing step, which is applied to the small $2 \times 2 \times 2$ supercell. The idea of using the small cell is that the Monte–Carlo simulated configuration can be used as an input for a new SLEC run. We start with a configuration, which is assumed to be a candidate for the ground state and gradually increase its Monte–Carlo temperature up to a certain value and then gradually decrease it until the configuration freezes in the lowest energy state. This new configuration is energy-minimized, and its energy and the frequency numbers are added to the set of previously simulated structures. The new least squares solution is then obtained and the Monte–Carlo annealing is repeated with the new values of the *J*s, A_{12} and A_{21} parameters. Typically, a few iterations are needed for the *J*s to converge to values consistent with the correct ground state. This procedure relies on the assumption that the empirical model (GULP) predicts the correct ground state.

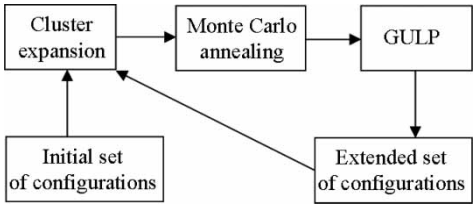

Figure 2. The feed-back algorithm which improves the accuracy of the cluster expansion in predicting ground state configurations.

However, this did not happen in the majorite case: the *J*s converged, but the low-energy Monte–Carlo configuration fluctuated between two structures with identical pair expansions, but very different GULP energies. One of these configurations corresponded to the correct $I4_1/a$ ground state, while the other one to an unknown triclinic, C2/c, structure with a much higher lattice energy. Since these structures had identical pair expansions, the *J*s fit was not able to predict the energies of both of them accurately, but resulted in the same compromise value. The C2/c configuration was subjected to the randomization procedure and 60 new randomized configurations were added to the original set of configurations. Figure 3 shows the *J*s fit to the whole set of configurations. The low accuracy of the fit suggests that the pair expansion misses some important

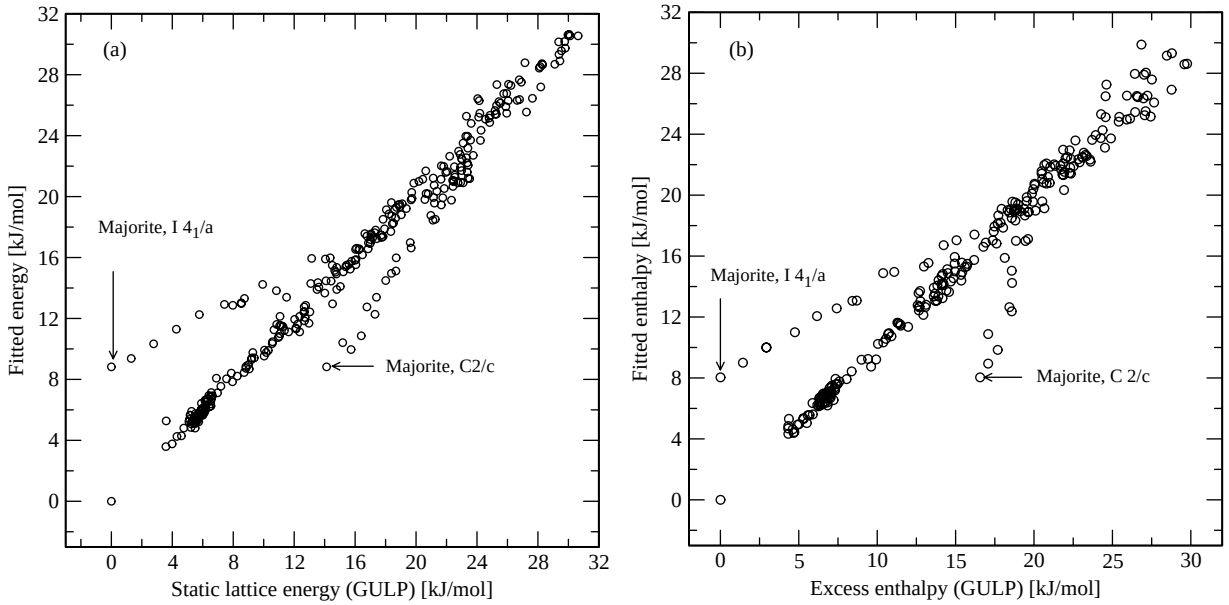

Figure 3. Correlation between the energies (a) and enthalpies (b) calculated with GULP and predicted with the pair cluster expansion. The enthalpies were calculated at 20 GPa.

physics. One can easily recognize that I4$_1$/a and C2/c structures are identical only in terms of the octahedral distribution. In fact, the C2/c structure can be obtained from the I4$_1$/a structure with a parallel shift of all octahedral atoms while leaving all other atoms fixed (figure 4). One can also observe that this shift destroys the tetragonal symmetry of the whole lattice: the 4-fold axes in the I4$_1$/a phase pass through the centers of the tetrahedral clusters of octahedral atoms, where all octahedral atoms are the same, and through the Si$^{[4]}$ sites, that center these clusters. In C2/c, the tetragonal symmetry is lost because the "all-same" tetrahedral clusters are swapped with the clusters that do not possess 4-fold symmetry. Since the C2/c structure has a higher lattice energy than I4$_1$/a, one can assume that the "all-same" arrangement with the Si$^{[4]}$ in the center has a lower energy than the all-same arrangement around an empty site.

In fact, the octahedral atoms in garnet form a perfect BCC lattice, which can be built by close packing of tetrahedral clusters. There are 6 such tetrahedra per one octahedral site. In garnets only 1/4 of these tetrahedra are filled with Si$^{[4]}$ atoms, the other 3/4 of the clusters are empty. This means that the octahedral distribution in garnets is made of two different types of tetrahedral clusters, filled and empty. This observation immediately suggests a new form of the cluster expansion, which is able to reflect the energetic difference of these cluster types:

$$E_i \approx \frac{1}{2}\sum_n z^{(n)} P_{\mathrm{AB}^{(n)}} J_n + \sum_{i,j,k,l}\left(P^{\mathrm{Va}}_{ijkl} - 3P^{\mathrm{Si}}_{ijkl}\right) Q_{ijkl} + E_0 \quad (5)$$

The first term in this equation describes the interactions within the pairs, while the second term reflects the tendency

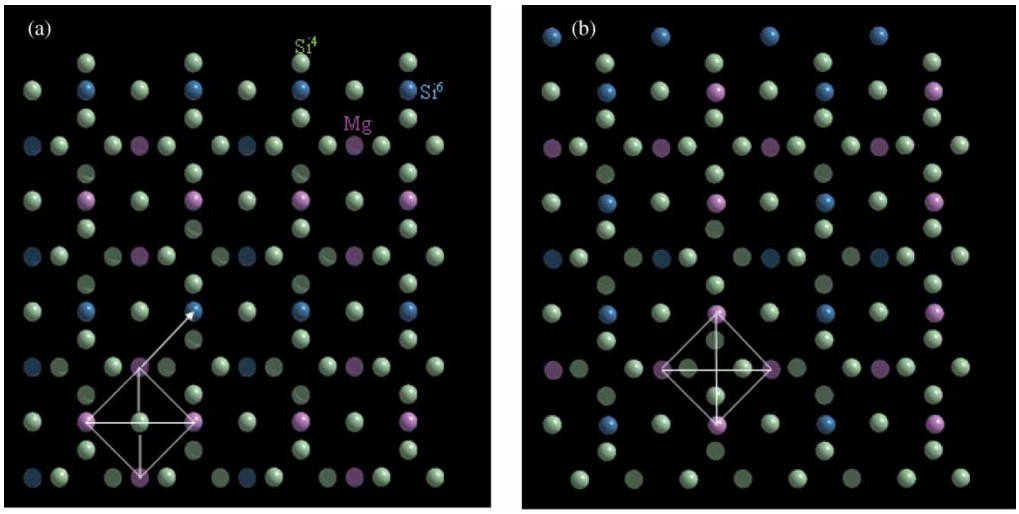

Figure 4. The I4$_1$/a (a) and C2/c (b) majorites viewed along the 4-fold axis of the tetragonal phase. The tetragonal symmetry is lost when MgMgMgMg and SiSiSiSi tetrahedral clusters move away from the centering Si$^{[4]}$ atoms. The image is prepared using the GDIS software [48].

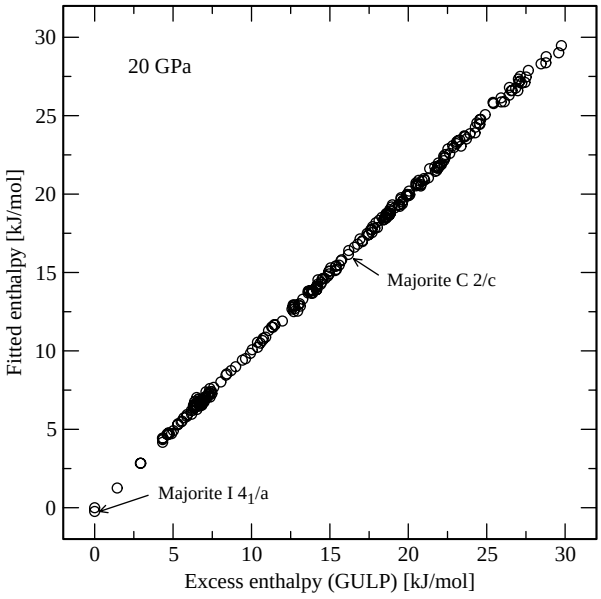

Figure 5. Correlation between the excess enthalpies calculated with GULP at 20 GPa and predicted with the J–Q expansion. A similarly good correlation is observed for the energies calculated at zero pressure.

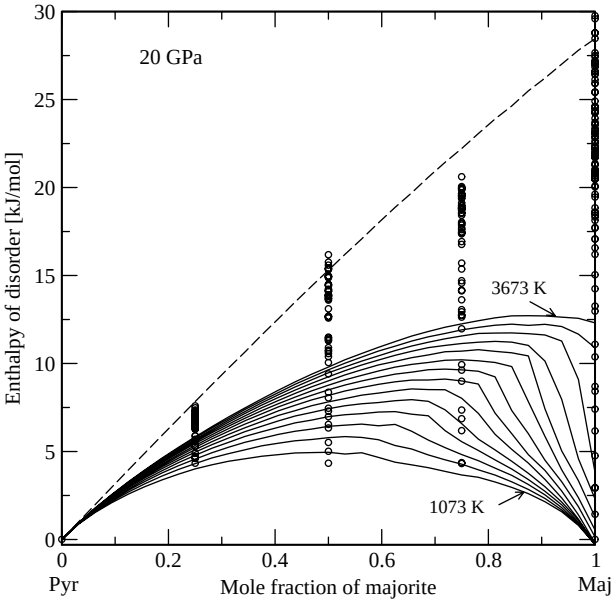

Figure 6. Enthalpy of disorder predicted with Monte–Carlo simulation (solid lines). The dashed line shows the enthalpy at the complete disorder or infinitely high temperature. Circles correspond to the excess energies of randomized configurations calculated with GULP. All values are per formula unit with one octahedral atom (6 oxygens).

of a tetrahedral group to locate itself either around $Si^{[4]}$ or an empty site. The P_{ijkl} and a_{ijkl} denote the probability (frequency) and the multiplicity of the tetrahedral group $ijkl$, where $i,j,k,l \in \{\mathrm{Al, Si, Mg}\}$. The factor of 3 is needed to equalize the numbers of the filled and vacant sites. With each $ijkl$ group we associate an energetic Q_{ijkl} constant. There are 21 symmetrically and chemically distinct groups. However, we have observed that when all 21 Q_{ijkl} constants are allowed to vary in the fit, their magnitudes become unreasonably large and some values correlate strongly with each other. We then arbitrarily fixed six of the constants at a value of zero and varied only the remaining 15 constants. The reduction to the 15-term expansion resulted in reasonable (small) values of the Q constants (table 4) and did not lead to any noticeable decrease in the fit accuracy compared to the 21-term expansion. Figure 5 shows the fit accuracy of the 15-term expansion. Apparently, the accuracy of J–Q expansion is sufficient for the energies of $I4_1/a$ and C2/c structures to be correctly distinguished. The J–Q expansion thus provides the possibility to greatly increase the speed of energy calculation without a significant loss in the accuracy. This in turn makes it feasible to efficiently simulate a Boltzmann probability distribution of the octahedral atoms with the Monte–Carlo method.

2.5 *Monte–Carlo simulations*

Monte–Carlo simulations have been performed using a $4 \times 4 \times 4$ supercell with periodic boundary conditions (1024 octahedral sites) with our own code. The swapping of sites has been performed according to the Metropolis algorithm. The energy differences between the subsequent steps have been calculated using equation (5). The temperature dependent properties have been calculated on a grid of 32 different compositions across the pyrope–majorite binary in the interval of 1073–3673 K with a step of 200 K. Each point in the T–X space was annealed for 500,000 Monte–Carlo steps and additional 500,000 steps were used for the calculation of the averages. The whole procedure was repeated twice, with the J–Q sets corresponding to 0 and 20 GPa. The results of both calculation runs are qualitatively similar and therefore we plot only the 20-GPa set. Figure 6 shows the isotherms of the excess configurational enthalpy together with the original set of energies calculated via the use of explicit interatomic potentials. It is clear that even at 3673 K the octahedral distribution significantly deviates from a random one. The breaks in the isotherms reflect the cubic/tetragonal transition. The LRO parameter variation across the transition was specially investigated at the majorite composition (figure 7). The LRO parameter has been defined as follows:

$$Q_{\mathrm{od}} = \frac{P_{\mathrm{A}\alpha} - P_{\mathrm{A}\beta}}{P_{\mathrm{A}\alpha} + P_{\mathrm{A}\beta}}, \qquad (6)$$

where $P_{\mathrm{A}\alpha}$ and $P_{\mathrm{A}\beta}$ are the probabilities of finding A atom (e.g. Mg) in two dissimilar octahedral sites. These two sites become structurally distinct in the tetragonal majorite [9]. However, these probabilities (frequencies) cannot be directly determined from the site occupancies derived from the Monte–Carlo simulations because the LRO fluctuates between the three equally possible orientations. Therefore, we have calculated the LRO parameter indirectly from the probabilities of AA pairs. The pair probabilities are much less affected by the spontaneous changes in the LRO orientation. Statistical theories of LRO suggest [49], that at short distances the pair probabilities are functions of both short-range order

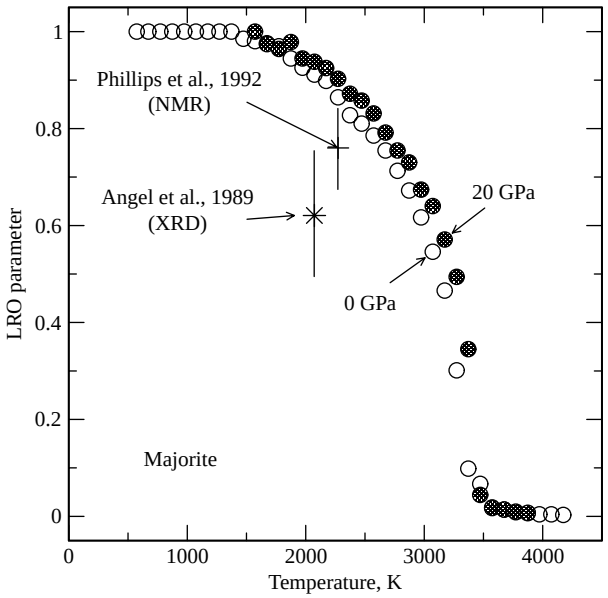

Figure 7. The temperature dependence of the long-range order parameter at 0 pressure and 20 GPa as calculated from Monte–Carlo simulations (circles). The cross and star denote the experimental data.

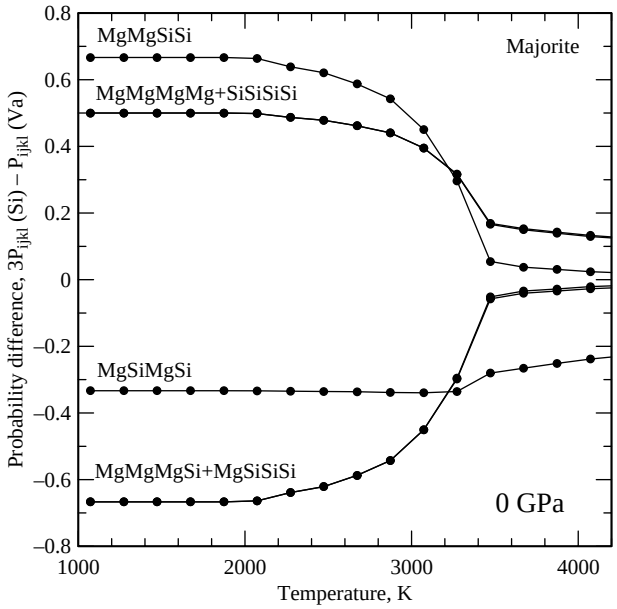

Figure 8. The probability difference between two different four-atom clusters predicted with the Monte–Carlo simulations. Below the transition temperature the proportion shifts in favour of the clusters consistent with the 4-fold symmetry.

(SRO) and LRO parameters. However, the SRO correlations rapidly vanish with distance and by measuring the AA probability at the maximum separation in the Monte–Carlo supercell one can be fairly sure that the SRO contribution is insignificant. (This distance was equal to 22.89 Å in our simulations.) Therefore,

$$P_{\mathrm{AA}} = P_{\mathrm{A}\alpha}P_{\mathrm{A}\beta} = P_{\mathrm{A}}^2(1 + Q_{\mathrm{od}})(1 - Q_{\mathrm{od}}^2)$$

$$= \frac{(1 - Q_{\mathrm{od}}^2)}{4} \tag{7}$$

From equation (7), one can easily recalculate Q_{od} (figure 7). One observes that the predicted degree of LRO at 2000°C is in good agreement with the experimental result of Phillips *et al.* [10] subject to the assumption that the measured quantity corresponds to the synthesis temperature. LRO completely disappears at about 3300 K at 0 GPa and at 3450 K at 20 GPa. The transition can be also visualized by monitoring the probabilities of the two types of tetrahedral clusters of octahedral sites; those with the $Si^{[4]}$ in the middle and the vacant ones. The difference of these probabilities exhibits a striking change at the transition temperature (figure 8).

2.6 Thermodynamic integration

It has been shown [18,19,50] that the configurational free energy can be calculated from Monte–Carlo averaged excess energies using the method of λ-integration:

$$F = F_0 + \int_0^{\lambda} \langle E \rangle_{\lambda} \mathrm{d}\lambda \tag{8}$$

In this equation, F_0 corresponds to the free energy of mixing of the solid solution with zero ordering energy, which can be calculated theoretically:

$$F_0 = TR(x_{\mathrm{Mg}} \ln x_{\mathrm{Mg}} + x_{\mathrm{Si}} \ln x_{\mathrm{Si}} + x_{\mathrm{Al}} \ln x_{\mathrm{Al}}) \tag{9}$$

The integral describes the contribution to the free energy from the energy (or the enthalpy in the case of a nonzero pressure), $\langle E \rangle$, when it changes from the state of complete disorder to the state of equilibrium order. To calculate $\langle E \rangle_{\lambda}$ for a state with an intermediate degree of order defined by certain value of λ, $0 < \lambda < 1$, one scales the *J*s and *Q*s

$$J_n^{\lambda} = \lambda J_n, \quad Q_{ijkl}^{\lambda} = \lambda Q_{ijkl} \tag{10}$$

and simulates Boltzmann's distribution constrained with J_n^{λ} and Q_{ijkl}^{λ}. Effectively, the scaling means that the probabilities of microstates become more random than in the non-scaled case. $\langle E \rangle_{\lambda}$ is then calculated using equation (5) with nominal (not scaled) values of *J*s and *Q*s by taking a simple average over a sufficient number of the equilibrated configurations. The aim of the scaling is to make the distribution more random without decreasing the strength of the interactions. In our simulations, λ was gradually increased from 0 to 1 with a step of 0.025. The integral was calculated using Simpson's method. The configurational entropy was calculated with the equation

$$S = \frac{(F - \langle E \rangle)}{T} \tag{11}$$

where $\langle E \rangle$ is the average excess energy (or enthalpy) calculated with $\lambda = 1$. Figure 9 shows the configurational entropy in the interval of 1073–3673 K. This function is severely affected by SRO and LRO. Evidently, the cationic distribution tends to the one-sublattice regime at low concentrations of majorite and at high temperatures.

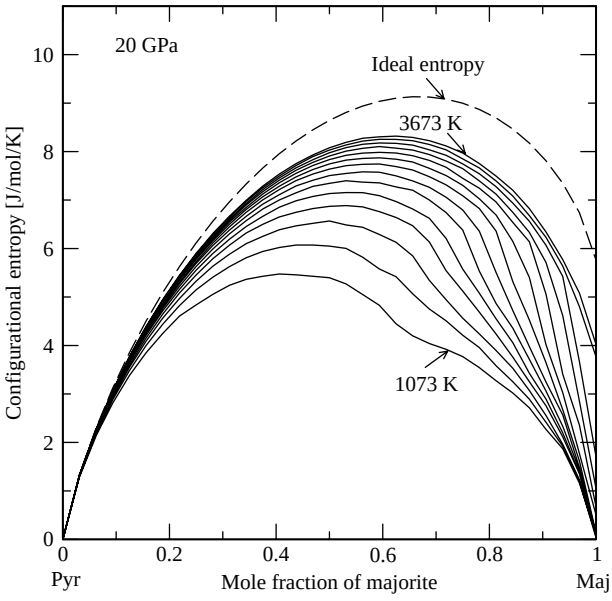

Figure 9. The configurational entropy of the octahedral site (per 1 mole of octahedral atoms) calculated using the method of thermodynamic integration. Dashed line shows the ideal entropy.

The two-sublattice regime is observed only at very low temperatures and at very majorite-rich compositions. The behaviour of the entropy at intermediate compositions cannot easily be predicted from simple model assumptions. Figure 10 shows the free energy of mixing at 20 GPa in the same interval of temperature. The excess values are calculated with respect to the mixture of pyrope and fully ordered majorite. One observes that the excess free energy of mixing of majorite deviates significantly from zero only at temperatures above 2673 K. This is the effect of disorder in majorite. One can also see that the miscibility gap starts to develop along the cubic–tetragonal boundary at about 2500 K and $x_{\mathrm{maj}} = 0.8$. At zero pressure this temperature is about 500 K lower. Curvature analysis of the free energies, combined with the order–disorder analysis, permits the drawing of the T–X phase diagram (figure 11).

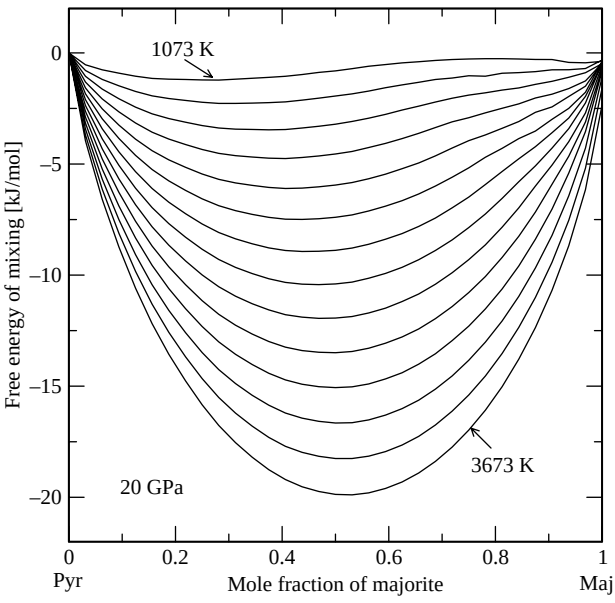

Figure 10. The free energy of mixing and calculated using the method of thermodynamic integration.

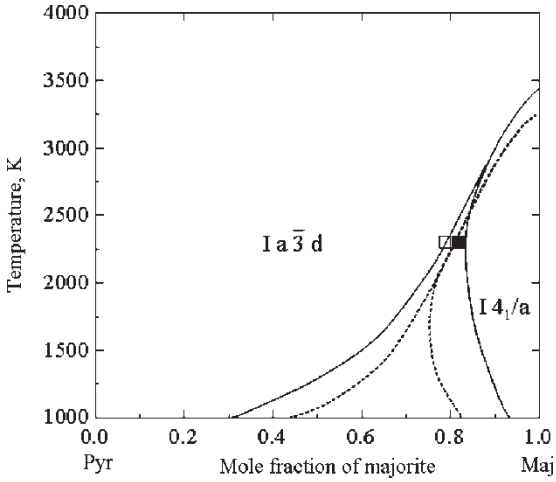

Figure 11. The temperature–composition phase diagram calculated based on the results of the Monte–Carlo simulations. (All other non-garnet phases are suppressed). The solid curve shows the result for 20 GPa, while the dashed line shows the phase boundaries at zero pressure. The squares represent the experimental results of Heinemann *et al.* [11]: open and filled squares correspond to the samples, which after the quench showed cubic and tetragonal symmetries, respectively.

2.7 *Activity–composition relations*

The free energy calculations suggest that the effect of disorder in majorite becomes significant only above 2673 K, i.e. at temperatures significantly exceeding the hypothetical mantle geotherm [3]. Therefore, we limit our activity–composition model to the 1073–2673 K interval. We have extracted the excess free energies of mixing from the Monte–Carlo energies and fitted them with a Redlich–Kister polynomial of the 6th order. Polynomials of lower order were not able to describe the curvature

Table 5. Coefficients of the Redlich–Kister polynomial for the excess free energy in the pyrope–majorite solid solution.

N	A_{1n} (kJ/mol)	$A_{2n} \times 10^{-3}$ (kJ/mol/K)	$A_{3n} \times 10^{-6}$ (kJ/mol/K^2)
1	20.7761	2.91736	−2.3053
2	−11.1357	19.77231	−5.979
3	−17.4504	22.02424	−4.9062
4	14.7575	−24.45104	8.7821
5	40.7301	−36.20679	8.1251
6	−13.7634	19.75529	−6.5512
7	−17.2006	10.69285	−1.4385
N	B_{1n} (kJ/mol)	$B_{2n} \times 10^{-3}$ (kJ/mol/K)	$B_{3n} \times 10^{-6}$ (kJ/mol/K^2)
1	−0.6976	2.1641	−0.3205
2	3.1557	−0.0637	0.1517
3	−0.2216	9.8304	−3.9812
4	−16.0881	20.3068	−5.5879
5	−24.0941	1.1400	4.6094
6	23.0833	−26.5699	7.2069
7	37.4186	−16.7439	0.0

of the free energy isotherms in the vicinity of the order/disorder transition.

The fitting was performed separately with the data for 0 and 20 GPa. The excess free energies were calculated with respect to the ideal one-site molecular solid solution. Our activities thus describe the mixing effect scaled to a single octahedral site. Table 5 plots the coefficients of the Redlich–Kister polynomial for the calculation of the excess free energy of the solid solution in the ranges of 1073–2673 K and 0–20 GPa. The A_{kn} set gives the coefficients corresponding to 0 GPa and the B_{kn} set gives the difference between the Redlich–Kister fit at 20 and 0 GPa. The free energies of mixing corresponding to any pressure of interest in the range of 0–20 GPa can be interpolated using the A_{kn} and B_{kn} coefficients with the equation

$$G_{\text{excess}} = x_1 x_2 \sum_{n=1}^{7} C_n (x_2 - x_1)^{n-1} \tag{13}$$

where

$$C_n = \sum_{k=1}^{3} \left(\frac{A_{kn} + PB_{kn}}{20} \right) T^{k-1} \tag{14}$$

and where T is measured in K and P in GPa. Equations (13), (14) will probably be reasonably accurate at pressures slightly above 20 GPa. Figure 12 plots the activity–composition relations at 20 GPa. The activities of pyrope and majorite are very much perturbed by the cubic/tetragonal transition and by the miscibility gap, which develops along the transition line. Comparing the figures 10 and 11, one observes that the simple polynomial equation is not enough robust for the description of the narrow gap at the high temperatures. This drawback of the model would not be significant in the majority of petrological applications though.

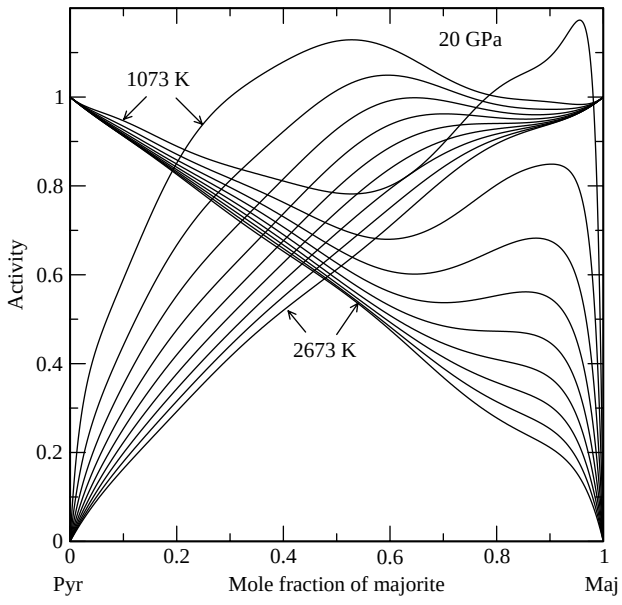

Figure 12. The activity–composition relations in the pyrope–majorite system consistent with the excess free energies described by equations (13), (14).

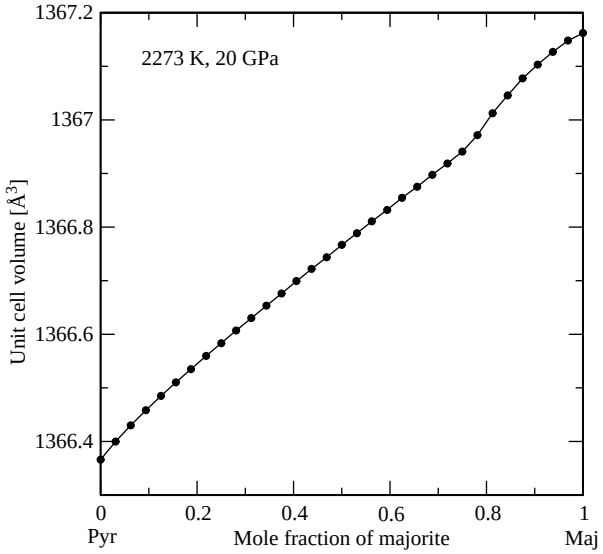

Figure 13. The variation of equilibrium volume along the binary at 2273 K and 20 GPa predicted with the volumetric cluster expansion.

2.8 Equilibrium volume

The relaxed volumes of the 260 configurations have been calculated using GULP through energy minimization calculations. The excess volumes have been cluster expanded with an equation analogous to equation (5). This has made it possible to find a set of pair and quaternary volumetric constants, which approximates the volume of any configuration. These constants have been used to monitor the equilibrium volume during the course of the Monte–Carlo simulations and to calculate the average volumes along the binary at different pressures and temperatures. Figure 13 shows the result for 20 GPa and 2273 K. The shape of the volume isotherm compares well with the measurements of Heinemann *et al.* [11] performed on a series of samples synthesized at 19 GPa and 2273 K. The predicted and experimental curves both show that the cubic/tetragonal transition leads to a slight, but noticeable, increase in the volume. Heinemann *et al.* [11] observed the break at $x_{\text{maj}} = 0.8$, which is in very good agreement with the calculated value of $x_{\text{maj}} = 0.75$.

3. Discussion

The developed statistical-thermodynamic model helps in understanding the driving forces which make the tetragonal majorite more stable than other possible ordered structures with the same composition. Table 4 shows that the strongest ordering pair interactions occur at the 1st, 2nd and 3rd neighbor distances. The electrostatic origin of these forces becomes clear when comparing the values of the Js corresponding to Al–Si, Al–Mg and Mg–Si interactions. Obviously, the strength of the interaction

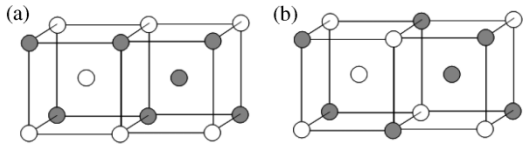

Figure 14. The arrangement of octahedral cations in $I4_1/a$ (a) and $P4_1$ 32 (b) majorites.

correlates with the charge difference within the pairs of cations: the Mg–Si interaction is always stronger than those of Al–Si and Al–Mg. The arrangement of the octahedral cations can be easily visualized as a BCC lattice, with two dissimilar cubic clusters centred on Si and Mg, respectively (figure 14a). Although it is possible to design a structure (figure14b) with an even larger number of the 2nd Mg–Si pairs than in $I4_1/a$ majorite, it will have a too low number of the 3rd-neighbor Mg–Si pairs. Our calculations show that this structure, with a symmetry of $P4_132$, is significantly less stable than the tetragonal majorite. The tetragonal majorite is certainly the best choice considering the advantage of having the maximum number of the 3rd-neighbor Mg–Si pairs and a not too low a number of the 2nd-neighbor pairs. However, as it was noted above, the optimum configuration of the octahedral cations can have a different relationship with regard to the underlying sublattice of the $Si^{[4]}$ atoms. The stabilization of the tetragonal majorite relative to the alternative C/2c phase probably occurs due to the interactions of the octahedral cations with the $Si^{[4]}$ atoms. In order to understand these interactions, it is convenient to visualize the BCC lattice as a superposition of the near-neighbor four-atom clusters of octahedral cations. One quarter of these clusters contain a $Si^{[4]}$ atom in the middle and the other three quarters are vacant. Our simulations suggest (figure 8) that the MgMgMgMg, SiSiSiSi and MgMgSiSi have a greater affinity to the $Si^{[4]}$ atoms than MgMgMgSi, SiSiSiMg and MgSiMgSi clusters. Since the centering of the first three clusters with a $Si^{[4]}$ atom is consistent with the 4-fold symmetry, the $I4_1/a$ majorite is more stable than the C2/c majorite.

The present calculations constrain the phase diagram and the activity–composition relations in the pyrope–majorite system at the conditions which cover the probable stability range of majorite in the transition zone. The main question is how accurate these calculations are. The predicted degree of LRO in tetragonal majorite (figure 7) is in good agreement with the data of Phillips *et al.* [10] obtained on a sample prepared at 2000°C and 17.7 GPa. The sample of Angel *et al.* [9] synthesized at 1800°C and 17 GPa falls slightly outside the trend. However, the authors concede that the result of their X-ray site occupancy refinement "must be treated with extreme caution because the scattering factors of Mg and Si are very similar". From bond lengths considerations they conclude that the degree of Mg, Si order is probably larger than that obtained from site refinement. The comparison of our results with those of Phillips *et al.* [10] and Angel *et al.* [9] is valid only if the experimental data essentially represent equilibrium properties, i.e. if the majorites were synthesized within the stability field of the tetragonal phase. However, Hatch and Ghose [12], Heinemann *et al.* [11] and Tomioka *et al.* [15] argue that the ordering to the tetragonal phase occurs during quenching such that the cubic/tetragonal boundary would lie significantly lower than the temperature of synthesis, and certainly significantly lower than our transition temperature (~3000°C). The authors have based their arguments on the observation of merohedral and pseudomerohedral twins generated by the loss of symmetry elements due to the ordering transition. Such transformation twins suggest that the majorites first crystallized with cubic symmetry. However, we will argue that the mere occurrence of transformation twins may not necessarily imply that the crystals have passed a transformation boundary during quenching. In fact, the metastable formation of a higher symmetry disordered structure within the stability field of the low temperature ordered form is not an unusual occurrence; it is to be expected if the starting materials are reactive [51].

Two examples may be given. The first one concerns the $C\bar{1}/I\bar{1}$ transition in Ca-rich plagioclases. The ordering transition leads to an alternation of the Al and Si atoms and thus produces superstructure reflections (so-called *b*-reflections) which may be used to image type *b* anti-phase domains in the TEM. Note that in contrast to the ordering transition in majorite which is translationengleich, but klassenungleich and as such is associated with the development of twins, the anorthite transition is klassengleich, but translationenungleich so that anti-phase domains are generated. In natural anorthites (An > 95%), although *b*-reflections are observed, no type *b* anti-phase domains can be imaged. Obviously, these anorthites directly crystallized with the ordered stable $I\bar{1}$ structure. In contrast, anorthite samples synthesized below the melting temperature do show type *b* domains although they crystallized in the stability field of the $I\bar{1}$ phase [52,53]. In the experiments of Kroll and Müller [53], the domains strongly increased in size with annealing time. Therefore, they certainly did not develop during the quench lasting only for seconds. This suggests that the synthetic anorthites first crystallized in a higher symmetry phase ($C\bar{1}$) and only then developed the $I\bar{1}$-type ordering at the annealing temperature. It is now agreed that also in natural anorthites with An-contents less than 95% showing type *b* domains nucleation of the domains occurred in a metastable $C\bar{1}$ albite matrix leading to the stable $I\bar{1}$ structure without crossing a transformation boundary (Smith and Brown [54], p. 89).

Another well-documented example is the case of Mg-cordierite which when synthesized from glass always forms the hexagonal high form (no LRO) within the stability field of the orthorhombic ordered structure [55–58]. The first-formed hexagonal phase has no domain structures. Continued annealing within the orthorhombic stability field produces a modulated structure and ultimately a twinned orthorhombic fully Al, Si ordered cordierite.

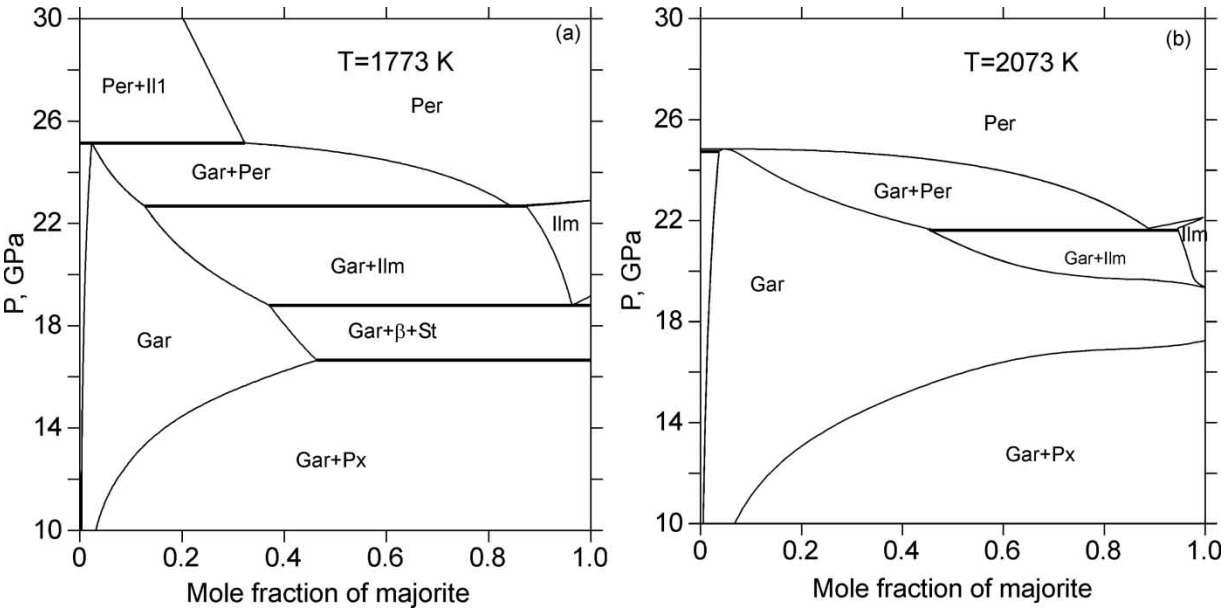

Figure 15. The phase relations in the pyrope–majorite system at (a) 1773 K and (b) 2073 K.

The discussion suggests that it is worth reconsidering the arguments of Hatch and Ghose [12] and Heinemann *et al.* [11]. Although the occurrence of twins suggests the existence of a cubic precursor, it is clear that the presence of twinning is not an indication that the material had ever been within the stability field of the high symmetry phase. We suggest that the cubic phase orders to the stable tetragonal phase immediately after crystallization. The tetragonal phase is characterized by the prevalence of MgMgMgMg, SiSiSiSi and MgMgSiSi tetrahedral clusters centred on $Si^{[4]}$ atoms. Presumably, during the initial stages of growth the clusters form with equal probability around both the $Si^{[4]}$ sites and the vacant sites leading to cubic symmetry and only then their proportion changes in favour of the Si sites leading to tetragonal symmetry.

One can argue that the empirical potential calculations might not be sufficiently accurate for predicting energy differences between configurations with different states of order, and thus the calculated transition temperatures could be significantly off. The comparison of our SLEC and *ab initio* calculations shows that the *ab initio* results suggest a larger difference in the energies of cubic and tetragonal majorites. If we assume that the *ab initio* values represent the correct answer, then the real energetic difference between ordered and disordered majorites should be even larger than that predicted by the SLEC and thus the cubic/tetragonal transition would occur at an even higher temperature than we have here predicted. However, we observe that the present SLEC results are in very good agreement with the data of Heinemann *et al.* [11], assuming that these data constrain true equilibrium. The predicted enthalpies of mixing are in good agreement with the available calorimetric data of Akaogi *et al.* [4] and Yusa *et al.* [5]: figure 6 predicts that the enthalpy of mixing of a Maj60 sample synthesized at 1273 K is about 11 kJ/mol per 12-oxygen formula unit, which compares well with the value of 12 ± 3.0 kJ/mol, estimated for this composition by Yusa *et al.* [5]. This agreement suggests that the present model is reasonably correct.

The present results might be questioned based on the lack of the evidence for a miscibility gap in phase equilibrium studies. However, the miscibility gap could be detected in a phase equilibrium study only if the both exsolved phases are stable at the experimental conditions. Our phase equilibrium calculations for the pyrope–majorite binary system (figure 15) suggest that the miscibility gap does not affect the topology of the pressure–composition diagram at temperatures lower than 1600°C. In these calculations, aided with the Thermo-Calc program [59], we have used the thermodynamic database of Fabrichnaya *et al.* [3] and the presently developed activity–composition model for the garnet phase. The gap is absent in the 1773 K diagram because it occurs at compositions that are not stable with respect to the other high-pressure mineral assemblages, such as pyrope-rich garnet + clinopyroxene, garnet + wadsleyite + stishovite and garnet + ilmenite. In the 2073 K set the gap is not revealed because at temperatures above 1873 K our Redlich–Kister model does not reproduce the small inflection in the free energy of the solid solution associated with the transition, although this inflection is present in the Monte–Carlo results. A narrow gap separating the cubic and tetragonal phases could be possibly observed experimentally at about 1800°C, where the majoritic garnet becomes stable over a wide-range of compositions. However, the experiments at such conditions are extremely challenging.

4. Conclusions

Atomistic simulations have allowed the investigation of the behaviour of mixing functions in the pyrope–majorite system in great detail and thus to calculate

the activity–composition relations consistently with the cubic/tetragonal transition. The model predicts that the transition occurs through a miscibility gap, which widens with the decrease in the temperature. The calculations suggest that the gap does not affect the topology of phase relations below 1600°C, where the majorite-rich phase is not stable with respect to other high-pressure mineral assemblages. However, if the mantle geotherm rises above 1800°C in the transition zone, it can cross the cubic/tetragonal transformation boundary and the associated with the transformation narrow miscibility gap. The heterogeneity of the garnet phase related to the miscibility gap and the twins related to the cubic/tetragonal transformation might significantly alter rheological properties of the lowest interval of the transition zone. These conclusions should be tested for systems containing Fe and Ca.

Acknowledgements

The majority of the results included in this publication have been developed as illustration materials for the lecture course "Introduction to Computer Simulations of Minerals" read during the Spring semester 2005 at the University of Münster by AP and VVL. Ulrik Hans, Jürgen Hansmann, Elis Hoffman, Arne Janßen and Dominik Niedermeier are thanked for asking tough questions and for the help in the computation. The support of the Deutsche Forschungsgemeinschaft (grant Wi 1232/14-2) is greatly acknowledged. JDG would like to thank the Government of Western Australia for funding under the Premier's Research Fellowship program.

References

[1] G. Fiquet. Mineral phases of the Earth's mantle. *Z. Kristallogr.*, **216**, 248 (2001).
[2] T. Gasparik. *Phase Diagrams for Geoscientists. An Atlas of the Earth's Interior*, Springer-Verlag, Berlin, Heidelberg (2003).
[3] O.B. Fabrichnaya, S.K. Saxena, P. Richet, E.F. Westrum. *Thermodynamic Data, Models and Phase Diagrams in Multicomponent Oxide Systems*, Springer-Verlag, Berlin (2004).
[4] M. Akaogi, A. Navrotsky, T. Yagi, S. Akimoto. Pyroxene–garnet transformation: thermochemistry and elasticity of garnet solid solutions, and applications to a pyrolite mantle. In *High-Pressure Research in Mineral Physics*, M.H. Manghnani, Y. Syono (Eds.), pp. 251–260, Am. Geophys. Union, Washington, DC (1987).
[5] H. Yusa, M. Akaogi, E. Ito. Calorimetric study of $MgSiO_3$ garnet and pyroxene: heat capacities, transition enthalpies, and equilibrium phase relations in $MgSiO_3$ at high pressures and temperatures. *J. Geophys. Res.*, **48**, 6453 (1993).
[6] M. Akaogi, S. Akimoto. Pyroxene–garnet solid solution equilibria in the systems $Mg_4Si_4O_4$–$Mg_3Al_2Si_3O_{12}$ and $Fe_4Si_4O_4$–$Fe_3Al_2Si_3O_{12}$ at high pressures and temperatures. *Phys. Earth Planet. Interiors*, **15**, 90 (1977).
[7] M. Kanzaki. Ultrahigh-pressure phase relations in the system. *Phys. Earth Planet. Interiors*, **49**, 168 (1987).
[8] T. Kato, M. Kumazawa. Garnet phase of $MgSiO_3$ filling the pyroxene–ilmenite gap at very high temperatures. *Nature*, 316 (1985).
[9] R.J. Angel, L.W. Finger, R.M. Hasen, M. Kanzaki, D.L. Weidner, R.C. Liebermann, D.R. Veblen. Structure and twinning of single crystal $MgSiO_3$ garnet synthesized at 17 GPa and 1800°C. *Am. Mineral.*, **74**, 509 (1989).
[10] B.L. Phillips, D.A. Howell, R.J. Kirkpatrick, T. Gasparik. Investigation of cation order in $MgSiO_3$-rich garnet using ^{29}Si and ^{27}Al MAS NMR spectroscopy. *Am. Mineral.*, **77**, 704 (1992).
[11] S. Heinemann, T. Sharp, F. Seifert, D.C. Rubie. The cubic–tetragonal phase transition in the system majorite ($Mg_4Si_4O_{12}$)–pyrope ($Mg_3Al_2Si_3O_{12}$), and garnet symmetry in the Earth's transition zone. *Phys. Chem. Minerals*, **24**, 206 (1997).
[12] D.M. Hatch, S. Ghose. Symmetry analysis of the phase transition and twinning in $MgSiO_3$ garnet: implications to mantle mineralogy. *Am. Mineral.*, **74**, 1221 (1989).
[13] Y. Wang, T. Gasparik, R.C. Liebermann. Modulated microstructure in synthetic majorite. *Am. Mineral.*, **78**, 1165 (1993).
[14] T. Gasparik. Phase relations in the transition zone. *J. Geophys. Res.*, **95**, 15751 (1990).
[15] N. Tomioka, K. Fujino, E. Ito, T. Katsura, T. Sharp, T. Kato. Microstructures and structural phase transition in $(Mg,Fe)SiO_3$ majorite. *Eur. J. Mineral.*, **14**, 7 (2002).
[16] R.J. Harrison, S.A.T. Redfern, J. Smith. The effect of transformation twins on the seismic frequency mechanical properties of polycrystalline $Ca_{1-x}Sr_xTiO_3$ perovskite. *Am. Mineral.*, **88**, 574 (2003).
[17] M.A. Carpenter, J.D.C. McConnell. Experimental delineation of the $C\bar{1}/I\bar{1}$ transformation in intermediate plagioclase feldspars. *Am. Mineral.*, **69**, 112 (1984).
[18] E.R. Myers, V. Heine, M.T. Dove. Some consequences of Al/Al avoidance in the ordering of Al/Si tetrahedral framework structures. *Phys. Chem. Minerals*, **25**, 457 (1998).
[19] M.T. Dove. Computer simulations of solid solutions. In *Solid Solutions in Silicate and Oxide Systems of Geological Importance. EMU Notes in Mineralogy*, Ch. Geiger (Ed.), Vol. 3, pp. 245–249, Eötvös University Press, Budapest (2001).
[20] A. Bosenick, M.T. Dove, E.R. Myers, E.J. Palin, C.I. Sainz-Diaz, B.S. Guiton, M.C. Warren, M.S. Craig, S.A.T. Redfern. Computational methods for the study of energies of cation distributions: applications to cation-ordering phase transitions and solid solutions. *Mineral. Mag.*, **65**, 193 (2001).
[21] M.S. Warren, M.T. Dove, E.R. Myers, A. Bosenick, E.J. Palin, C.I. Sainz-Diaz, B.S. Guiton, M.C. Craig, S.A.T. Redfern. Monte–Carlo methods for the study of cation ordering in minerals. *Mineral. Mag.*, **65**, 221 (2001).
[22] U. Becker, A. Fernandez-Gonzales, M. Prieto, R. Harrison, A. Putnis. Direct calculation of thermodynamic properties of the barite/celestite solid solution from molecular principles. *Phys. Chem. Minerals*, **27**, 291 (2000).
[23] U. Becker, K. Pollock. Molecular simulations of interfacial and thermodynamic mixing properties of the grossular–andradite garnets. *Phys. Chem. Minerals*, **29**, 52 (2002).
[24] V.L. Vinograd, M.H.F. Sluiter, B. Winkler, A. Putnis, U. HÅlenius, J.D. Gale, U. Becker. Thermodynamics of mixing and ordering in the pyrope–grossular solid solution. *Mineral. Mag.*, **68**, 101 (2004).
[25] J.D. Gale. Empirical potential derivation for ionic materials. *Phil. Mag. B*, **73**, 3 (1996).
[26] J.D. Gale. GULP—a computer program for symmetry adapted simulations of solids. *J. Chem. Soc. Faraday Trans.*, **93**, 629 (1997).
[27] M.J. Sanders, M. Leslie, C.R. Catlow. Interatomic potentials for SiO_2. *J. Chem. Soc., Chem. Commun.*, **19**, 1271 (1984).
[28] A. Patel, G.D. Price, M.J. Mendelsson. A computer-simulation approach to modelling the structure, thermodynamics and oxygen isotope equilibria of silicates. *Phys. Chem. Minerals*, **17**, 690 (1991).
[29] B. Winkler, M.T. Dove, M. Leslie. Static lattice energy minimization and lattice dynamics calculations on aluminosilicate minerals. *Am. Mineral.*, **76**, 313 (1991).
[30] V.L. Vinograd, M.H.F. Sluiter, B. Winkler, A. Putnis, J.D. Gale. Thermodynamics of mixing and ordering in silicates and oxides from static lattice energy and *ab initio* calculations. In *First-Principles Simulations: Perspectives and Challenges in Mineral Sciences. Deutsche Gesellschaft für Kristallographie. Berichte aus Arbeitskreisen der DFK*, M. Warren, A. Oganov, B. Winkler (Eds.), Vol. 14, pp. 143–151 (2004).
[31] J.D. Bass. Elasticity of Minerals, Glasses, and Melts. In *Mineral Physics & Crystallography. A Handbook of Physical Constants. Am. Geophys. Union, AGU Reference Shelf Ser., 2*, Th.J. Ahrens (Ed.), pp. 45–63 (1995).

[32] R.T. Downs, M. Hall-Wallace. The American mineralogist crystal structure database. *Am. Mineral.*, **88**, 247 (2003).
[33] R.E.G. Pacalo, D.L. Weidner. Elasticity of majorite $MgSiO_3$ tetragonal garnet. *Phys. Earth. Planet. Interiors*, **99**, 145 (1997).
[34] S.V. Sinogeikin, J.D. Bass. Elasticity of majorite and majorite–pyrope solid solution to high pressure: Implications for the transition zone. *Geophys. Res. Lett.*, **29**(2), 4-1 (2002).
[35] P. Hohenberg, W. Kohn. Inhomogeneous electron gas. *Phys. Rev.*, **136**, B864 (1964).
[36] W. Kohn, L.J. Sham. Self-consistent equations including exchange and correlation effects. *Phys. Rev.*, **140**, A1133 (1965).
[37] R.G. Parr, W. Yang. *Density-functional theory of atoms and molecules*, Oxford University Press, Oxford (1989).
[38] E.S. Kryachko, E.V. Ludena. Energy density functional theory of many-electron systems. *Understanding Chemical Reactivity*, Vol. 4, Kluwer Academic Publishers, Dordrecht (1990).
[39] R.O. Jones, O. Gunnarsson. The density functional formalism, its applications and prospects. *Rev. Mod. Phys.*, **61**, 689 (1989).
[40] J.P. Perdew, K. Burke, M. Ernzerhof. Generalized gradient approximation made simple. *Phys. Rev. Lett.*, **77**, 3865 (1996).
[41] T.C. Leung, C.T. Chan, B.N. Harmon. Ground-state properties of Fe, Co, Ni and their monoxides: results of the generalized gradient approximation. *Phys. Rev.*, **B44**, 2923 (1991).
[42] J. Goniakowski, J.M. Holdender, L.N. Kantarovich, M.J. Gillan, J.A. White. Influence of gradient corrections on the bulk and surface properties of TiO_2 and SnO_2. *Phys. Rev.*, **B53**, 957 (1996).
[43] D.R. Hamman. Generalized gradient theory for silica phase transitions. *Phys. Rev. Lett.*, **76**, 660 (1996).
[44] D. Vanderbilt. Soft self-consistent pseudopotentials in a generalized eigenvalue formalism. *Phys. Rev.*, **B41**, 7894 (1990).
[45] G. Kresse, J. Hafner. Norm-conserving and ultrasoft pseudopotentials for first-row and transition elements. *J. Phys.: Condens. Matter*, **6**, 8245 (1994).
[46] C.A. McCommon, N.L. Ross. Crystal chemistry of ferric iron in $(Mg,Fe)(Si,Al)O_3$ majorite with implications for the transition zone. *Phys. Chem. Minerals*, **30**, 206 (2003).
[47] V.L. Vinograd. Configurational entropy of binary silicate solid solutions. In *Solid Solutions in Silicate and Oxide Systems of Geological Importance. EMU Notes in Mineralogy*, Ch. Geiger (Ed.), Vol. 3, pp. 245–249 (2001).
[48] S.D. Fleming, A.L. Rohl. GDIS: A visualization program for molecular and periodic systems. *Z. Kristallogr.*, **220**, 580 (2005).
[49] V.L. Vinograd, A. Putnis. The description of Al, Si ordering in aluminosilicates using the cluster variation method. *Am. Mineral.*, **84**, 311 (1999).
[50] E.R. Myers. Al/Si ordering in silicate minerals. PhD thesis, Univ. of Cambridge (1999).
[51] M.A. Carpenter, A. Putnis. Cation order and disorder during crystal growth: some implications for natural mineral assemblages. In *Advances in Physical Geochemistry*, A.B. Thompson, D.C. Rubie (Eds.), Vol. 4, Springer-Verlag, Berlin (1985).
[52] M.A. Carpenter. Mechanisms and kinetics of Al–Si ordering in anorthite: I. Incommensurate structure and domain coarsening. *Am. Mineral.*, **76**, 1110 (1991).
[53] H. Kroll, W.F. Müller. X-ray and electron-optical investigation of synthetic high-temperature plagioclases. *Phys. Chem. Minerals*, **5**, 255 (1980).
[54] J.V. Smith, W.L. Brown. *Feldspar minerals. 1. Crystal structures, physical, chemical and microtextural properties*, Springer-Verlag, Berlin, Heidelberg (1988).
[55] A. Putnis. The distortion index in anhydrous Mg-cordierite. *Contrib. Mineral. Petrol.*, **74**, 135 (1980).
[56] A. Putnis, D.L. Bish. The mechanism and kinetics of Al, Si ordering in Mg-cordierite. *Am. Mineral.*, **68**, 60 (1983).
[57] A. Putnis, C.A. Fyfe, G.C. Gobbi. Al,Si ordering in cordierite using "magic angle spinning" NMR spectroscopy. I: ^{29}Si spectra of synthetic cordierites. *Phys. Chem Minerals*, **12**, 211 (1985).
[58] A. Putnis, E.S. Salje, S.A.T. Redfern, C.A. Fyfe, H. Strobl. Structural states of Mg-cordierite I: Order parameters from synchrotron X-ray and NMR data. *Phys. Chem. Minerals*, **14**, 446 (1987).
[59] B. Sundman, B. Jansson, J-O. Andersson. The Thermo-Calc databank system. *Calphad*, **9**, 153 (1985).